

## Patterns of electroconvection in a nematic liquid crystal

Michael Dennin,<sup>1</sup> David S. Cannell,<sup>2</sup> and Guenter Ahlers<sup>2</sup>

<sup>1</sup>*Department of Physics and Astronomy, University of California at Irvine, Irvine, California 92697-4575*

<sup>2</sup>*Department of Physics and Center for Nonlinear Science, University of California at Santa Barbara, Santa Barbara, California 93106*

(Received 31 January 1997; revised manuscript received 31 July 1997)

We present a survey of pattern formation in electroconvection of the nematic liquid crystal *4-ethyl-2-fluoro-4'-[2-(trans-4-pentylcyclohexyl)-ethyl] biphenyl* (I52) as a function of three control parameters: the applied voltage, applied frequency, and electrical conductivity of the sample. The patterns are dominated by oblique-roll states. Over the lower range of conductivity, the initial transition is a supercritical Hopf bifurcation which leads to four degenerate modes: right- and left-traveling zig and zag rolls. For higher values of the conductivity, the primary instability is a subcritical bifurcation to a single set of stationary oblique rolls. The convecting states exhibit a rich variety of patterns as a result of the interactions between the four modes, including states of spatiotemporal chaos and localized states. [S1063-651X(98)08301-9]

PACS number(s): 61.30.Gd, 47.54.+r, 47.52.+j, 47.20.-k

### I. INTRODUCTION

Convection in a shallow horizontal layer of an *isotropic* fluid heated from below is well known as Rayleigh-Bénard convection (RBC) [1]. It has been used extensively for the study of a great variety of pattern-formation phenomena [2]. For RBC, an infinite number of wave vectors, corresponding to all convection rolls with wave-vector modulus  $k_c$  and having all possible orientations, acquire positive growth rates at a critical value of the control parameter (in this case the temperature difference across the sample). Thus the patterns that form have no preferred orientation unless one is imposed by an inhomogeneity of the experimental cell. Complementary to this case is electroconvection in a thin layer of a nematic liquid crystal, a paradigm for pattern formation in *anisotropic* systems [3–6].

Nematic liquid crystal molecules have an inherent orientational order relative to each other, but no positional order, and the direction parallel to the average molecular alignment is referred to as the director  $\hat{n}$  [7]. A properly prepared sample can have  $\hat{n}$  oriented uniformly along a particular axis in the plane of the fluid layer. This case is known as planar alignment. An ac voltage of amplitude  $V$  and frequency  $f$  is applied across the sample using transparent conducting films on the inner surfaces of the glass plates. For certain nematic liquid crystals, there is a critical value  $V_c$  of  $V$  for which a transition from a spatially uniform state to a convecting state occurs. The nature of the convection pattern depends on the electrical conductivity of the sample. In order to achieve sufficiently high electrical conductivities, pure liquid crystals must be doped with ionic impurities. The pattern generally will have a specific orientation relative to  $\hat{n}$  because only one or a small number of wave vectors  $\mathbf{k}_c$  acquire a positive growth rate at  $V_c$ . Interesting new bifurcation phenomena involving the orientation of these modes relative to  $\hat{n}$ , as well as pattern-formation phenomena above threshold involving nonlinear interactions between the modes, can occur. A great variety of spatiotemporal structures has been observed, including time-independent rolls [8,9], traveling waves [9–15],

defect chaos [11,16], chaos at onset [17,18], and localized states [10,18,19].

Many of the interesting features of anisotropic systems are the result of patterns formed by the superposition of a small number of plane-wave modes whose wave vectors form nonzero angles with respect to the director, i.e., oblique rolls. Because the orientation of  $\hat{n}$  defines an axis but does not distinguish right from left along that axis, we chose the following convention to describe plane-wave oblique rolls. As shown in Fig. 1, we took the  $x$  axis parallel to  $\hat{n}$ , with the  $z$  axis perpendicular to the plane of the sample. We chose to describe the patterns using wave vectors  $\mathbf{k}$  with positive  $x$  components, as shown. Patterns with  $0 < \Theta < \pi/2$  are designated zig rolls, and those with  $-\pi/2 < \Theta < 0$  are designated zag rolls. Here  $\Theta$  is the angle between  $\mathbf{k}$  and the positive  $x$  axis. (Note, the standard nomenclature for  $\Theta = 0$  is to refer to such patterns as normal rolls.) There is nothing in the system that can serve to distinguish zig and zag states with the same  $|\mathbf{k}|$  and  $|\Theta|$ . Consequently, such states must acquire a positive growth rate at the same value of applied voltage, and for this reason, we refer to them as degenerate. It is the *nonlinear* interactions between *degenerate* zig and zag modes which lead to a rich variety of interesting phenomena [6,13,14],

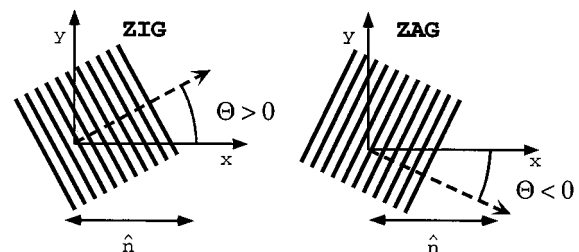


FIG. 1. The conventions used to define  $\Theta$  for zig and zag rolls are illustrated here. The  $x$  and  $y$  axes are in the plane parallel to the glass plates of the electroconvection cell, and the director is along the  $x$  axis. The positive  $x$  direction has been chosen to be to the right. The thick lines represent plane-wave oblique rolls, and the dashed arrows represent the wave vectors of these rolls.

including spatiotemporal chaos at onset.

For electroconvection in our samples of the nematic liquid crystal *4-ethyl-2-fluoro-4'-[2-(trans-4-pentylcyclohexyl)-ethyl] biphenyl* (I52) with an electrical conductivity  $0.8 \times 10^{-8} \leq \sigma_{\perp} \leq 1.8 \times 10^{-8} \Omega^{-1} \text{ m}^{-1}$  ( $\sigma_{\perp}$  is the conductivity in the direction perpendicular to  $\hat{n}$ ), we found that the initial instability is a supercritical Hopf bifurcation, i.e., a continuous and nonhysteretic transition to a state with a characteristic frequency  $\omega_c$ . The bifurcation yields an oblique-roll state which involves four degenerate modes: left- and right-traveling zig and zag rolls [14,20]. At higher conductivities, the initial bifurcation is to a state of stationary zig or zag rolls. In this paper we report on a survey of *nonlinear* aspects of the system, namely, the patterns observed above onset. These patterns can be attributed to interactions between some or all of six modes: stationary, left-traveling, and right-traveling zig and zag rolls.

There are a number of reasons for studying the nonlinear patterns exhibited by electroconvection in I52. First, the *linear* properties of this system ( $V_c$ ,  $\mathbf{k}_c$ , and  $\omega_c$ ) have been explained quantitatively by the weak-electrolyte model [21] of electroconvection and are discussed in detail elsewhere [20]. Since the initial instability is supercritical over a wide parameter range, solutions to coupled Ginzburg-Landau equations derived from the weak-electrolyte model should quantitatively describe much of the rich behavior of this system above but close to threshold where amplitudes are small. Secondly, as the frequency of the applied voltage is increased, the angle of the oblique rolls,  $\Theta$ , goes to zero as the square root of that frequency. The value of the frequency at which  $\Theta=0$  is referred to as the Lifshitz point. For our samples of I52, the Lifshitz point occurred sufficiently above our experimental frequency range that  $\Theta \approx 30^\circ$  [20] in our experiments. So far as we know, this value of  $\Theta$  is greater than those for any previously studied material. This is the most likely source of the novel patterns we observed.

Among the patterns are three different examples of spatiotemporal chaos. For the purposes of this paper, spatiotemporal chaos refers to deterministic patterns with unpredictable spatial and temporal variations [2]. We considered patterns to be examples of spatiotemporal chaos if their correlation length was significantly smaller than the system size and their correlation time was finite. This is a relatively loose definition of spatio-temporal chaos, and further work is needed to fully characterize the examples discussed in this paper. One of the examples is a structure that is localized in the direction perpendicular to  $\hat{n}$ . We refer to this pattern as “worms” because of its spatial and temporal appearance [18] (see, for example, Fig. 7). The other two examples of spatiotemporal chaos are “extended” states, i.e., the pattern fills the sample. One consists of four degenerate traveling modes with amplitudes which vary irregularly in space and in time. It occurs at a primary supercritical bifurcation [17]. The other involves six modes, and occurs for values of  $V$  well above  $V_c$  via a secondary bifurcation. Another interesting aspect of this system is the existence of a secondary bifurcation from a single set of stationary oblique rolls to a pattern which is the superposition of *nondegenerate* zig and zag rolls, where nondegenerate refers to the fact that the roll states have different values of  $|\Theta|$ .

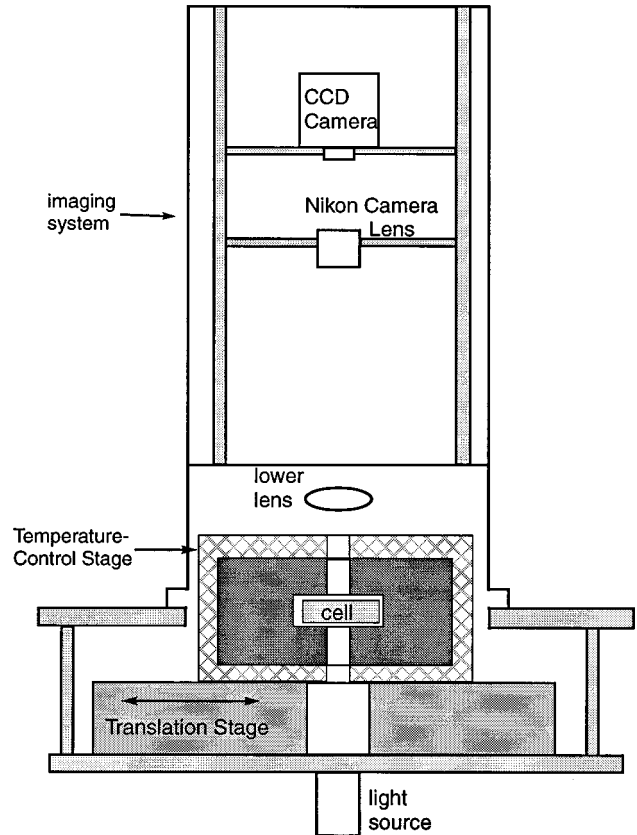


FIG. 2. A schematic drawing of the apparatus.

The rest of this paper is organized as follows. Section II describes the experimental apparatus and outlines the techniques used to analyze the images. In Sec. III we present the results, and Sec. IV contains a summary and suggests some future avenues of exploration.

## II. EXPERIMENTAL METHOD, IMAGE ANALYSIS, AND FLUID PROPERTIES

The electroconvection apparatus consists of a shadowgraph apparatus for visualization and a temperature-controlled sample stage (see Fig. 2). The shadowgraph apparatus is a modified version of the one described in Ref. [22]. It consists of two parts: a light source mounted below and an imaging system mounted above the sample stage.

The light source is a 660-nm light-emitting diode coupled into a 50- $\mu\text{m}$  diameter optical fiber. The optical fiber is 2 m long with a numerical aperture of 0.22. The light is converted into a parallel beam by a 10-mm-diameter achromatic lens with a 20 mm focal length. A dichroic sheet polarizer is placed between the light source and the sample cell and can be rotated with respect to the cell.

The imaging system consists of two lenses and a charge-coupled device (CCD) camera which are mounted in a 1.2-m-high aluminum tube. The lower lens is a 20-mm-diameter achromat with a 52.7-mm focal length. This lens is fixed in place 6.63 cm above the cell. The second lens is a Nikon 50-mm  $f/1.4$  camera lens. The Nikon lens and CCD camera are mounted on separate movable carriages. The design of the carriages allows the relative position of the Nikon lens

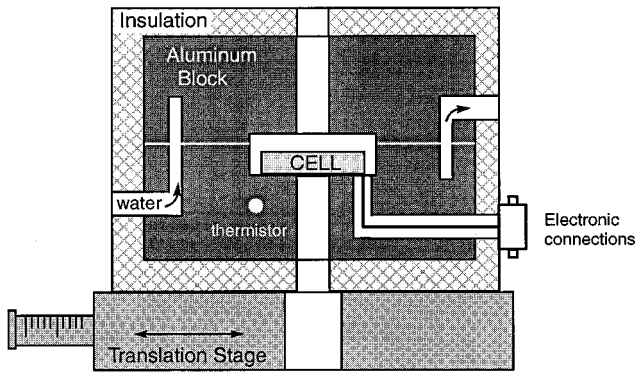


FIG. 3. A schematic drawing of the temperature-controlled stage containing the sample.

and CCD camera on the one hand and the position of the Nikon lens and camera as a unit on the other to be adjusted independently. The combined magnification of the two lenses ranges from  $1\times$  to  $20\times$ . The image is digitized using an 8-bit gray scale, and divided pixel by pixel by a reference image which is taken below the onset of convection. The image division removes most of the inhomogeneities in the optics. For display purposes, the divided image is rescaled to cover the range 0–255. For numerical analysis, the unscaled divided image is used.

The sample stage is shown in more detail in Fig. 3. It is mounted on an  $x$ - $y$  translation stage with  $1\text{-}\mu\text{m}$  resolution. This permits the selection of a particular part of a large sample for detailed study. It also allows the calibration of the magnification of the shadowgraph system by imaging a reference object in two lateral positions with a known relative displacement. The stage consists of a 9.78-cm-diameter aluminum cylinder of height 6.78 cm and wrapped with 0.64 cm of insulating foam. The cylinder is split approximately along its horizontal midplane, and near its center it contains a cavity which holds the sample. To allow for illuminating the sample from below and viewing it from above, there is a 1.40-cm-diameter hole along the axis of the cylinder. The hole is closed at the top and bottom with glass windows to reduce or avoid convection of the air within it. A 0.318-cm-wide and 2.54-cm-high circular channel with an inner radius of 3.56 cm is located with its midplane at the midplane of the aluminum cylinder. This channel surrounds the sample cavity. Temperature-controlled water flows through it and provides a temperature stability of the aluminum block of  $\pm 1$  mK (rms). The upper limit to the operating temperature of the apparatus is around  $70^\circ\text{C}$ .

The cell thickness  $d$  was set by Mylar gaskets and was uniform to  $0.5\ \mu\text{m}$ . The observations reported here are from four different cells with spacings of  $28\ \mu\text{m}$ ,  $28\ \mu\text{m}$ ,  $30\ \mu\text{m}$ , and  $54\ \mu\text{m}$ . We will refer to these cells as cell 28-1, 28-2, 30, and 54, respectively. It is necessary to distinguish nominally identical samples (28-1 and 28-2) because of variations in the electrical conductivities of the samples. The planar alignment was achieved with rubbed polyimide layers that were spin coated onto the slides. Further details of the cell construction are discussed in Ref. [23].

To achieve the required electrical conductivities, the nematic liquid crystal I52 was doped with 2% by weight molecu-

lar iodine [24]. We measured  $\sigma_{\perp}$  for each sample as a function of applied angular frequency  $\Omega$ . Here  $\sigma_{\perp}(\Omega) = (d/A)\text{Re}[I(\Omega)/V(\Omega)]$  where  $I(\Omega)$  is the measured complex current in response to the applied  $V(\Omega)$ ,  $d$  is the cell thickness, and  $A$  is the area of the electrode. We used two methods to measure  $\sigma_{\perp}$ . One employed a standard capacitor bridge and lock-in amplifier to measure the real and imaginary components of  $I(\Omega)$ . The other was described in Ref. [15]. The accuracy of our measurements of  $\sigma_{\perp}$  was approximately 2% and was limited by difficulties measuring  $A$  and  $d$ . However, for a given cell these quantities are fixed, and we were able to measure changes in  $\sigma_{\perp}$  with a precision of a few tenths of a percent. A detailed discussion of  $\sigma_{\perp}$  and its frequency dependence is given in Ref. [23]. There is a strong frequency dependence of  $\sigma_{\perp}$  as  $\Omega \rightarrow 0$ , but for  $\Omega/2\pi > 25$  Hz,  $\sigma_{\perp}$  is constant within the limits of our measurements. For the results reported here, the values of  $\sigma_{\perp}$  were measured using  $\Omega/2\pi = 25$  Hz.

The conductivity of an individual cell could be varied by up to a factor of 3 by changing the temperature over the range  $44^\circ\text{C}$ – $60^\circ\text{C}$ . Cells with different values of  $\sigma_{\perp}$  for a given temperature were obtained by varying the amount of iodine used to dope the I52. In addition, a small linear drift in the conductivity with time meant that different values of  $\sigma_{\perp}$  at a fixed temperature could be studied for a particular cell. Comparing the results from different cells and at different times showed that the observed series of transitions depended primarily on conductivity rather than on temperature. However, the actual voltage at which each transition occurred was often temperature dependent. We believe this is the result of other material parameters, particularly the anisotropy of the dielectric constant, changing with temperature. For this reason, data taken for different temperatures but having the same conductivity are not quantitatively comparable.

Two important material parameters are  $\epsilon_a = \epsilon_{\parallel} - \epsilon_{\perp}$  and  $\sigma_a = \sigma_{\parallel} - \sigma_{\perp}$  where  $\epsilon_{\parallel}$  ( $\sigma_{\parallel}$ ) and  $\epsilon_{\perp}$  ( $\sigma_{\perp}$ ) are the principal components of the dielectric constant (conductivity) tensor parallel and perpendicular to the director. For I52 in the temperature range  $T = 44^\circ\text{C}$ – $60^\circ\text{C}$ ,  $\epsilon_a$  was previously measured [15,25] to range from  $-0.03$  to  $0$ .

We measured  $\sigma_{\perp}$  directly, but did not measure  $\sigma_{\parallel}$ . Therefore, to determine  $\sigma_a$ , we inferred  $\sigma_a/\sigma_{\perp}$  from comparisons between the predicted [20] value of  $V_c$  for zero applied frequency and the zero frequency limit of the measured values of  $V_c$ . The zero frequency limit of the measurements was determined by extrapolating the data for  $\Omega/2\pi \geq 25$  Hz. For the conditions of our experiments, the weak-electrolyte model [21] and the calculations in Ref. [4] predict the same values for  $V_c$ , so either calculation can be used. However, the comparison with the prediction of  $V_c$  is only valid for parameter values for which the primary bifurcation is known to be supercritical. Therefore this method is valid over the entire range of temperatures only when a sample is sufficiently doped such that  $\sigma_{\perp} \geq 0.7 \times 10^{-8} \Omega^{-1} \text{m}^{-1}$  for all  $T$  (see Sec. III). This limited our ability to determine the magnitude of  $\sigma_a$ . However, using a sample with a sufficient level of doping, we found  $\sigma_a/\sigma_{\perp} > 0$  over the entire temperature range. Presumably, the sign of  $\sigma_a/\sigma_{\perp}$  is not dependent on the dopant concentration; thus we assume that  $\sigma_a$  is

TABLE I. Summary of modes.

Mode	Representation	Range of angle ( $\Theta$ ) between director and $\mathbf{k}$
Stationary zig	$A(\mathbf{x},t)\cos[\mathbf{k}\cdot\mathbf{x}+\phi(\mathbf{x},t)]$	$0 < \Theta < \pi/2$
Right-traveling zig	$A(\mathbf{x},t)\cos[\mathbf{k}\cdot\mathbf{x}-\omega t+\phi(\mathbf{x},t)]$	$0 < \Theta < \pi/2$
Left-traveling zig	$A(\mathbf{x},t)\cos[\mathbf{k}\cdot\mathbf{x}+\omega t+\phi(\mathbf{x},t)]$	$0 < \Theta < \pi/2$
Stationary zag	$A(\mathbf{x},t)\cos[\mathbf{k}\cdot\mathbf{x}+\phi(\mathbf{x},t)]$	$-\pi/2 < \Theta < 0$
Right-traveling zag	$A(\mathbf{x},t)\cos[\mathbf{k}\cdot\mathbf{x}-\omega t+\phi(\mathbf{x},t)]$	$-\pi/2 < \Theta < 0$
Left traveling zag	$A(\mathbf{x},t)\cos[\mathbf{k}\cdot\mathbf{x}+\omega t+\phi(\mathbf{x},t)]$	$-\pi/2 < \Theta < 0$

positive for all of the patterns (even the localized ones for  $\sigma_{\perp} < 0.7 \times 10^{-8} \Omega^{-1} \text{ m}^{-1}$ ) reported on here. For a discussion of the other properties of I52, see footnote 25 of Ref. [20].

The patterns consisted of superpositions of roll-like modes each of which can be written as  $A_n(\mathbf{x},t)\cos[\mathbf{k}_n\cdot\mathbf{x}-\omega_n t+\phi_n(\mathbf{x},t)]$ , where  $n$  labels the modes. Here  $\mathbf{k}_n$  and  $\omega_n$  are the wave vector and the angular frequency of a given mode, and  $\mathbf{x}=(x,y)$  is the position vector in the plane of the fluid layer. The  $A_n(\mathbf{x},t)$  and  $\phi_n(\mathbf{x},t)$  are the slowly varying amplitude and phase of the pattern that describe variations on length and time scales that are large compared to those defined by  $|\mathbf{k}_n|$  and  $|\omega_n|$ , respectively. The six possible modes are listed in Table I. Having chosen the  $x$  axis parallel to the director, the angle between  $\mathbf{k}_n$  and the director is given by  $\Theta_n = \tan^{-1} q_n/p_n$  where  $p_n$  and  $q_n$  are the  $x$  and  $y$  components of  $\mathbf{k}_n$ , respectively. As discussed, we use the convention that states with angles in the range  $0 < \Theta < \pi/2$  are designated zig states and those with  $-\pi/2 < \Theta < 0$  are designated zag states. Two roll states, labeled by  $n=1$  and  $n=2$ , are considered degenerate when  $|\omega_1|=|\omega_2|$ ,  $|\mathbf{k}_1|=|\mathbf{k}_2|$ , and  $|\Theta_1|=|\Theta_2|$ .

We analyzed the shadowgraph images using the spectral density  $S(\mathbf{k},\omega)$  (the square of the modulus of the space-time Fourier transform of the divided image). When the time evolution or only a snapshot at one time was of interest, the transform in space only was used and  $S(\mathbf{k},t)$  was computed. Occasionally, we may refer to  $S(\mathbf{k},t)$  as the ‘‘spatial power spectrum’’ of the image. When time-averaged amplitudes were desired, we would take the time average  $S(\mathbf{k})$  of  $S(\mathbf{k},t)$ . All transforms were normalized so that Parseval’s theorem was obeyed, i.e., so that the variance of the image in real space is equal to the total power in Fourier space. Thus time and space averages  $\langle A_n^2 \rangle$  of the squares of the mode amplitudes  $A_n$  could be obtained by summing the contributions to  $S(\mathbf{k})$  in the vicinity of the relevant peak. Wave vectors were determined by calculating the first moment of  $S(\mathbf{k})$ , again using only the vicinity of the relevant peak (see, for instance, Refs. [26,27]). The correlation length and correlation time for a given mode were taken to be the inverse of the width of the corresponding peak in the spectral density. The amplitude of the variation of the director in the  $z$  direction,  $\theta$ , was estimated from the mode amplitudes  $\langle A_n^2 \rangle$  using [28]  $\theta = (A_n/4)(d/\lambda)\{[2 - (n_e/n_o)^2]/[1 - (n_e/n_o)^2]\}$ . Here  $\theta$  is in radians;  $d$  is the cell thickness;  $\lambda$  is the wavelength of the pattern;  $A_n = (\langle A_n^2 \rangle)^{1/2}$ ; and  $n_e$  and  $n_o$  are the extraordinary and ordinary indices of refraction of

I52, respectively. This formula is based on geometric optics and derived in Ref. [28].

Demodulation was used to study the states of spatiotemporal chaos for which the behavior of  $A_n(\mathbf{x},t)$  is of particular interest. Demodulation consists of performing the space-time Fourier transform of a time series of images and setting the Fourier transform to zero everywhere except for a small region around the  $\mathbf{k}_n$  and  $\omega_n$  of interest. The inverse Fourier transform of this modified function is a complex function of space and time. Its real part corresponds to  $A_n(\mathbf{x},t)\cos[\mathbf{k}_n\cdot\mathbf{x}-\omega_n t+\phi(\mathbf{x},t)]$ , and its modulus is the desired  $A_n(\mathbf{x},t)$ . One can also demodulate single spatial images to find the amplitude as a function of position for the zig and zag rolls without distinguishing between right- and left-traveling states.

It should be pointed out that the shadowgraph method under many circumstances is highly nonlinear [28], and that for this reason the images seen in real space often can be quite misleading. We illustrate this in Fig. 4. The left portion shows a real-space image of a pattern for  $\epsilon = 0.066$  and  $\sigma_{\perp} = 1.0 \times 10^{-8} \Omega^{-1} \text{ m}^{-1}$ . Here  $\epsilon \equiv (V^2/V_c^2 - 1)$  is the reduced control parameter. The image gives the impression of a rect-

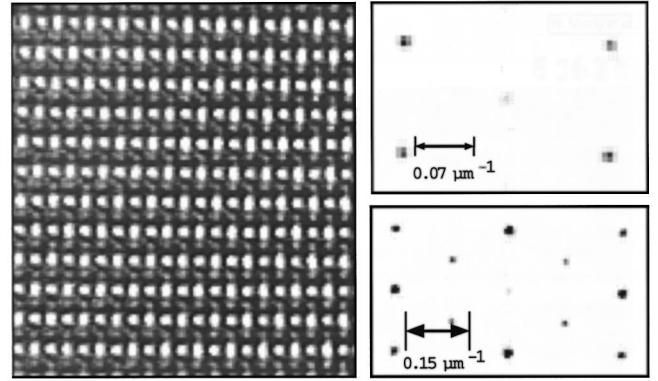


FIG. 4. The left portion is a typical shadowgraph image resulting from the superposition of zig and zag oblique rolls. It covers an area  $0.5 \text{ mm} \times 0.5 \text{ mm}$  in cell 28-2. For this image,  $\sigma_{\perp} = 1.0 \times 10^{-8} \Omega^{-1} \text{ m}^{-1}$  and  $\epsilon = 0.066$ . The image gives the appearance of a rectangular structure, with different characteristic length scales in the  $x$  and  $y$  directions. The upper right portion is the central region of the spatial power spectrum of the image. It shows that the fundamental wave vectors correspond to oblique rolls. The lower right portion shows a larger range of Fourier space, and reveals strong contributions from higher harmonics and sums and differences of the fundamental components. The origins of the spectra are at the image centers. The scales of  $k_x$  and  $k_y$  are given by the bars.

TABLE II. Summary of observed patterns.

Pattern name	Spatial extent	number of modes	Number of traveling modes	Relationship between zig and zag
Oblique	extended	1	0	NA
SO1	extended	2	0	same $ \Theta $
SO2	extended	2	0	different $ \Theta $
EC1	extended	4	4	same $ \Theta $
EC2	extended	6	4	same $ \Theta $
Worms	localized	(see text)	(see text)	NA

angular structure formed by the superposition of two sets of rolls. One set seems to have the roll axes horizontal (parallel to  $\hat{n}$ ) and the other vertical (normal to  $\hat{n}$ ), and they appear to have two different wavelengths. In order to gain a more objective understanding of the modes which contribute to the pattern we examine  $S(\mathbf{k}, t)$ . The central portion of  $S(\mathbf{k}, t)$ , given in the top right portion of Fig. 4, shows that the rectangular appearance of the pattern is illusory. The transform reveals contributions from zig and zag rolls, with wave vectors  $\mathbf{k}_1 = (p, q)$  and  $\mathbf{k}_2 = (p, -q)$ , respectively, and  $-\mathbf{k}_1$  and  $-\mathbf{k}_2$ , all with the same modulus  $k = \sqrt{p^2 + q^2}$ . The lower right part of Fig. 4 shows a larger portion of Fourier space. It reveals that, in addition to the fundamental components, there are strong contributions from  $\mathbf{k}_1 + \mathbf{k}_2 = (2p, 0)$  and  $\mathbf{k}_1 - \mathbf{k}_2 = (0, 2q)$  which are responsible for the appearance of the rectangular structure in real space with the two illusory length scales  $\pi/p$  and  $\pi/q$ .

We do not believe that the higher-order components of  $S(\mathbf{k}, t)$  arise from the fluid flow, but rather that they are an optical effect caused by the nonlinearities of the shadow-graph method. The existence of the second harmonics is easily understood in terms of the focusing of light due to variations of the index of refraction. The samples are illuminated with light polarized along the  $x$  axis. The index of refraction of the sample is a tensor and depends on the square of the angle  $\theta(x, y)$  in the  $x$ - $z$  plane between the director and the polarization. This variation of the index of refraction focuses light rays and produces an intensity modulation. The wavelength of this modulation corresponds to the width of one roll, or half the wavelength of the pattern. There is an additional focusing effect that is proportional to  $\theta(x, y)$  that produces a modulation with the wavelength of two rolls, or equal to that of the pattern. This effect is explained in detail in Ref. [28].

For all of the images shown here, the director is aligned horizontally (the  $x$  axis), and the gray-scaled plots of the power spectra have  $(p=0, q=0)$  in the centers of the images. We never found a measurable variation of the director in the  $x$ - $y$  plane. This was checked by observing the patterns through crossed polarizers.

### III. RESULTS

#### A. Pattern descriptions

We identified six different patterns. One of them, the worm state [18], is unique in that it is highly localized transverse to the director and much less strongly localized parallel to the director. The width of the worm state is on the order of

a wavelength [18]. Therefore this state is not a superposition of a finite number of modes with *slowly* varying amplitudes  $A(\mathbf{x}, t)$ . However, it may be useful to treat it as a superposition of a few modes with *strongly* varying amplitudes. Close inspection of the real-space images reveals two types of worms: those well approximated by a superposition of right-traveling zig and zag rolls, and those well approximated by left-traveling zig and zag rolls. In each case, the amplitude  $A(\mathbf{x}, t)$  of the modes varies strongly in the direction perpendicular to the director [18].

The other five patterns are spatially extended, and essentially fill the cell. They can be decomposed into sums of the modes listed in Table I with *slowly* varying amplitudes and phases. The modes that comprise a particular pattern were determined from the peaks in the spectral density  $S(\mathbf{k}, \omega)$ .

Three of the patterns are stationary ( $\omega=0$ ). Of these, the simplest is referred to as oblique rolls in keeping with standard nomenclature. The other two time-independent patterns may be decomposed into a superposition of stationary zig and zag rolls. We denoted these states as SO1 and SO2, with SO referring to ‘‘stationary oblique.’’ These two patterns differ in that the SO1 pattern is a superposition of degenerate zig and zag rolls, i.e., oblique rolls with the same  $|\Theta|$ , whereas the SO2 pattern results from a superposition of zig and zag roll with different  $|\Theta|$  (of nondegenerate modes). We observed the SO2 state only well above threshold, and not as the result of a primary bifurcation.

The remaining two extended states exhibited spatiotemporal chaos, and we denoted them as EC1 and EC2. Here EC refers to ‘‘extended chaotic.’’ The EC1 pattern was the result of a primary bifurcation and may be decomposed into right- and left-traveling zig and zag modes. The EC2 state consisted of all six possible modes, the two stationary ones and the four traveling ones. Therefore, even though  $|\mathbf{k}_i| = |\mathbf{k}_j|$  and  $|\Theta_i| = |\Theta_j|$  for all six modes, the EC2 state involves the superposition of nondegenerate modes. By definition, the stationary modes ( $\omega=0$ ) are not degenerate with the traveling modes ( $\omega \neq 0$ ) because  $|\omega_i| \neq |\omega_j|$ . As with the SO2 state, the other example of a superposition of nondegenerate modes, the EC2 state was only observed to arise from a secondary bifurcation. The fact that these two states are not observed at onset is reasonable. At  $V_c$ , one would only expect to observe states that are either composed of a single mode or are the superposition of degenerate modes.

For easy reference, the six patterns together with the modes underlying them are summarized in Table II.

#### B. Transitions between patterns

The parameter space for electroconvection is extremely large, and our choice of parameters was guided by a number

of factors. In principle, there are four easily accessible control parameters: the applied voltage  $V$ , the thickness of the cell  $d$ , the applied angular frequency  $\Omega$ , and the conductivity of the sample perpendicular to the director  $\sigma_{\perp}$ . Because we used sealed cells with a fixed thickness, we were not able to perform systematic studies as a function of  $d$ ; therefore we focused on the three parameters  $V$ ,  $\Omega$ , and  $\sigma_{\perp}$ .

Because many of the transitions between patterns are hysteretic, the path taken in parameter space to achieve a particular value of  $V$ ,  $\Omega$ , and  $\sigma_{\perp}$  is important. For this work, we chose to study the behavior as a function of the reduced control parameter  $\epsilon \equiv (V^2/V_c^2) - 1$ . Therefore  $\sigma_{\perp}$  and  $\Omega$  were only varied with  $V$  held at a value close to zero for which there was no pattern. For each value of  $\sigma_{\perp}$  and  $\Omega$ , a separate critical voltage  $V_c$  was measured.

Our results are reported in terms of the dimensionless frequency  $\Omega\tau_q$ . It has been shown experimentally [20] that  $V_c$  is a function of  $\Omega$  and  $\sigma_{\perp}$  only in the combination  $(\Omega/\sigma_{\perp})\epsilon_0\epsilon_{\perp}$ . This is in agreement with theoretical predictions [4,21]. The quantity  $(\Omega/\sigma_{\perp})\epsilon_0\epsilon_{\perp}$  is just the dimensionless frequency  $\Omega\tau_q$  where  $\tau_q$  is the charge relaxation time [25,29]  $\tau_q \equiv \epsilon_0\epsilon_{\perp}/\sigma_{\perp}$ . Here  $\epsilon_0$  is the permittivity of free space. Physically,  $\tau_q$  is the relaxation time with which a charge density fluctuation perpendicular to  $\hat{n}$  decays. Over the range of parameters used here for I52,  $\tau_q \approx 10^{-3}$  s.

Even though  $\Omega\tau_q$  depends on both  $\Omega$  and  $\sigma_{\perp}$ , the nonlinear properties of the pattern depended separately on  $\sigma_{\perp}$  and  $\Omega\tau_q$ . Theory [21] strongly suggests that this is due to a third dimensionless parameter that scales as  $\sigma_{\perp}d^2$ . General trends from our limited study of different  $d$  support this belief; however, theory provides a number of possible dimensionless parameters [21] that all scale as  $\sigma_{\perp}d^2$ . At present, there are insufficient data as a function of  $d$  to identify the correct parameter. Therefore we report our data as a function of  $\epsilon$ ,  $\Omega\tau_q$ , and  $\sigma_{\perp}$ , and make a note when a different value of  $d$  is used. This does introduce the complication that both  $\sigma_{\perp}$  and  $\Omega$  must be adjusted in order to vary  $\sigma_{\perp}$  for fixed  $\Omega\tau_q$ .

Even limiting our study to the three parameters  $\epsilon$ ,  $\Omega\tau_q$ , and  $\sigma_{\perp}$ , a large parameter space remains to be explored. Therefore we focus on one cut through the  $\epsilon$ - $\sigma_{\perp}$  plane located roughly in the middle of the range of  $\Omega\tau_q$ , at  $\Omega\tau_q = 1.34$ . The results of this study are summarized in Fig. 5. We also studied two cuts in the  $\epsilon$ - $\Omega\tau_q$  plane at fixed values of  $\sigma_{\perp}$ , involving two different samples. These are summarized in Fig. 6.

In terms of unscaled quantities, the applied voltage for these studies ranged from 5  $V_{\text{rms}}$  to 60  $V_{\text{rms}}$ . The applied frequency ranged from 25 Hz to 500 Hz, and the value of  $V_c$  ranged from  $V_c \approx 10$   $V_{\text{rms}}$  to  $V_c \approx 35$   $V_{\text{rms}}$ . The range of  $\Omega$  was fixed from above by the cutoff frequency [3]  $\Omega_c$ . Above  $\Omega_c$ , one observes a qualitatively different type of pattern formation known as dielectric convection [3]. For our samples,  $\Omega_c\tau_q \approx 3$ . The lower limit of applied frequency was chosen to be  $\Omega/2\pi = 25$  Hz to avoid the strong frequency dependence of  $\sigma_{\perp}$  as  $\Omega \rightarrow 0$ . For our samples,  $\Omega/2\pi = 25$  Hz corresponds to  $0.1 \leq \Omega\tau_q \leq 0.6$ , depending on  $\sigma_{\perp}$ . The upper limit on the conductivity range was set by our ability to dope I52. The lower limit was set by the decrease of  $\Omega_c$  with decreasing  $\sigma_{\perp}$ .

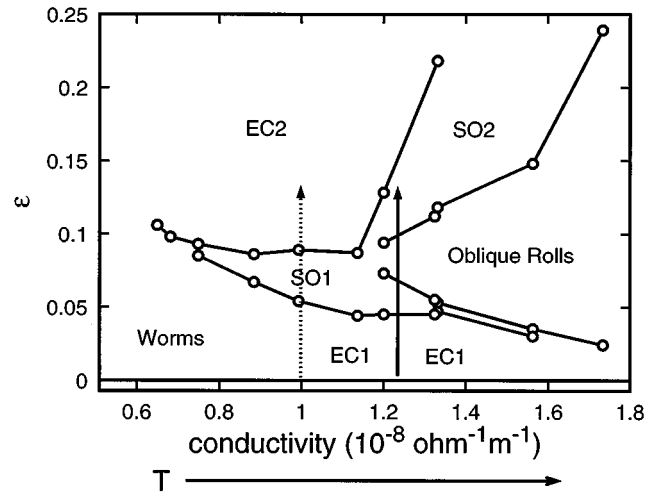


FIG. 5. The regions where the various patterns are observed as a function of  $\epsilon$  and  $\sigma_{\perp}$  at  $\Omega\tau_q = 1.34$  for the cell 28-2. Here  $\sigma_{\perp}$  (the conductivity perpendicular to the director) was varied by changing the temperature  $T$ , as indicated by the arrow below the abscissa, and  $\Omega\tau_q$  was held fixed by varying  $\Omega$ . The results were obtained using a temperature range from 44 °C to 59 °C. The solid vertical arrow corresponds to  $\sigma_{\perp} = 1.24 \times 10^{-8} \Omega^{-1} \text{ m}^{-1}$  and  $T = 54$  °C. The dashed vertical arrow at  $\sigma_{\perp} = 1.0 \times 10^{-8} \Omega^{-1} \text{ m}^{-1}$  and  $T = 49$  °C is an experimental path discussed in the text.

As discussed in the section on material parameters, there are a number of factors that limit quantitative comparisons

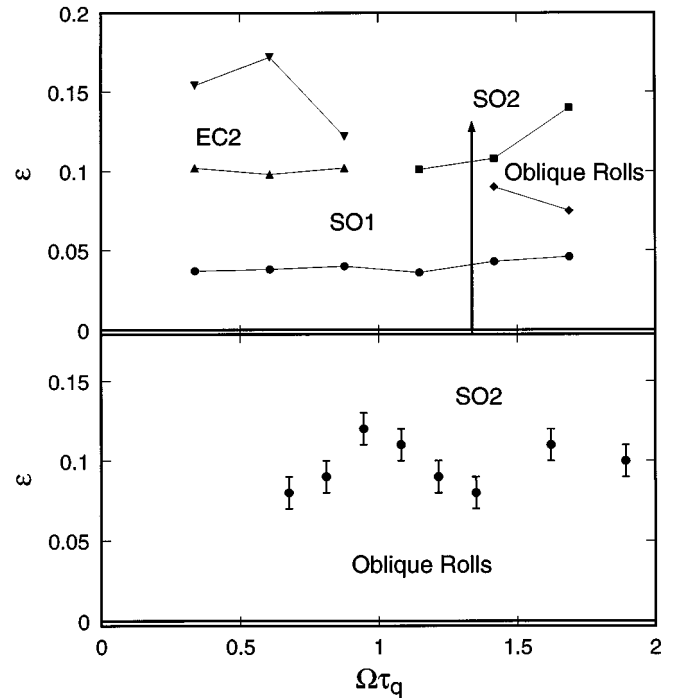


FIG. 6. The top portion of the figure shows the regions where the various patterns are observed as a function of  $\epsilon$  and  $\Omega\tau_q$  for  $T = 57$  °C in cell 28-2. For this plot,  $\Omega\tau_q$  was varied by changing  $\Omega$ , and  $\sigma$  was held fixed at  $1.24 \times 10^{-8} \Omega^{-1} \text{ m}^{-1}$ . The solid vertical arrow corresponds to  $\Omega\tau_q = 1.34$ , which was the value used for  $\Omega\tau_q$  in Fig. 5. The bottom portion of the figure shows the regions where the various patterns are observed as a function of  $\epsilon$  and  $\Omega\tau_q$  in the cell 28-1. Here  $\sigma_{\perp} = 2.2 \times 10^{-8} \Omega^{-1} \text{ m}^{-1}$  and  $T = 44$  °C.

between Figs. 5, 6(a), and 6(b). First, the results in Fig. 6(b) are from sample 28-1 and those in Figs. 5 and 6(a) are from sample 28-2. Recall that for different samples the same conductivity corresponds to different temperatures. Therefore, because of variations in other material parameters, the  $\epsilon$  values of the transitions are not quantitatively comparable between different samples. Similarly, because of the slow drift in conductivity with time, the same conductivity in Fig. 5 and Fig. 6(a) corresponds to slightly different temperatures. This shift in  $\sigma_{\perp}$  with time is the reason that the solid line used to mark the connection between Figs. 5 and 6(a) does not pass through actual data points on either plot. The only significant discrepancy is in the transition from the SO2 state to the EC2 state. This is due to the large slope of the SO2 to EC2 transition for  $\sigma_{\perp} \approx 1.24 \times 10^{-8} \Omega^{-1} \text{ m}^{-1}$ , the value of  $\sigma_{\perp}$  used to measure Fig. 6(a).

All of the boundaries in Figs. 5 and 6 were measured by quasistatically stepping the voltage. The system was equilibrated after each step in  $\epsilon$  for 15 minutes. This time was chosen to be long compared to the director relaxation time,  $\tau_d \approx 1$  s. The primary bifurcation lines ( $\epsilon=0$ ) in Figs. 5 and 6(a) were measured with steps of  $\delta\epsilon = 5 \times 10^{-4}$ , and the secondary transitions in these figures were measured by stepping  $\epsilon$  in steps of  $\delta\epsilon = 5 \times 10^{-3}$ . In Fig. 6(b), all of the boundaries were measured with a step size of  $\delta\epsilon = 0.01$ .

The discussion of the details of the transitions between patterns is divided into three sections. The first section reports on the primary bifurcations as a function of  $\sigma_{\perp}$ . The primary bifurcations to EC1 and to the worm state have been studied in detail and reported on previously [17,18,20]. We review the important characteristics of these transitions and report on measurements of a primary stationary bifurcation that occurs at higher values of  $\sigma_{\perp}$ . Second, the transition from EC1 to SO1 and from SO1 to EC2 will be discussed. In particular, quantitative measurements of the patterns along the path marked by the vertical dashed arrow in Fig. 5 will be reported. The third section will be a discussion of a number of qualitative features of the SO2 state, and the secondary transitions from the worm state.

### C. Initial bifurcations

For  $\sigma_{\perp} \leq 0.7 \times 10^{-8} \Omega^{-1} \text{ m}^{-1}$ , the initial bifurcation is directly to the worm state. The worms are localized in the direction perpendicular to  $\hat{n}$  and travel throughout the cell parallel to  $\hat{n}$ . They possess a distribution of lengths along the director, but their width (perpendicular to  $\hat{n}$ ) is unique for a given set of control parameters. Examples at one value of  $\epsilon$  and as a function of time are shown in Fig. 7. A more detailed description of this state was given elsewhere [18]. The worms are stable in the sense that they are destroyed only by traveling out of the cell or through interactions with other worms. Worms appear spontaneously from the conduction state at seemingly random locations. When a worm is born, it clearly involves a superposition of right- and left-traveling waves, leading to a standing-wave state. However, as the amplitudes of the modes within the worm grow, only the right- or the left-traveling waves survive. Thus each individual mature worm involves only right- or left-traveling zig and zag rolls. Worms of both types coexist in different spatial locations of the same sample. For the parameters we

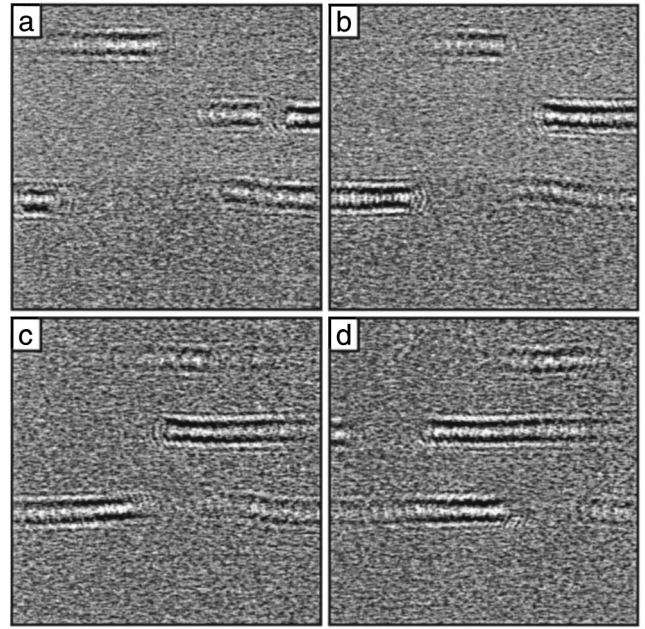


FIG. 7. Snapshots from a time series of the worm state at  $\epsilon = 0.012$  and  $\sigma_{\perp} = 0.6 \times 10^{-8} \Omega^{-1} \text{ m}^{-1}$  and  $T = 55^\circ \text{C}$  in cell 30. The images (a), (b), (c), and (d) were taken 60 s apart. Each image covers an area of  $0.17 \text{ cm} \times 0.17 \text{ cm}$ .

investigated, worms consisting of right- (left-) traveling rolls move to the left (right) with a speed about a tenth of the traveling-wave speed. Very near onset, worms are very rare and relatively short, with a relatively large spacing between them in the  $y$  direction (perpendicular to  $\hat{n}$ ).

As  $\sigma_{\perp}$  is increased, there is a change in the primary bifurcation. Instead of the worm state, EC1 is the initial state. However, the boundary between the worm regime and the EC1 state does not appear to be sharp. For values of  $\sigma_{\perp}$  near  $0.8 \times 10^{-8} \Omega^{-1} \text{ m}^{-1}$ , we observed both worms and the EC1 state for  $\epsilon$  as small as  $1 \times 10^{-3}$ . Neither state appeared to be a transient, as the system alternated between the two states aperiodically for up to 24 hours. However, for  $\sigma_{\perp} \geq 0.9 \times 10^{-8} \Omega^{-1} \text{ m}^{-1}$ , the initial transition is always to the EC1 state, and worms are no longer observed.

Measurements of the root-mean-square amplitude of the director deviation from perfect planar alignment demonstrate that the bifurcation to EC1 is supercritical. The amplitude increases continuously with  $\epsilon$ , and within the experimental resolution of  $\delta\epsilon = 5 \times 10^{-4}$ , there is no observable hysteresis. A typical example is given in Fig. 8. The steps in  $\epsilon$  are  $5 \times 10^{-4}$ . For  $\epsilon < 0$ , the rms amplitude had a nearly constant small value which was consistent with thermally induced fluctuations below onset [30].

A snapshot of a relatively large area of the EC1 state is shown in the top portion of Fig. 9. One can see that there are spatial regions where either the zig or the zag mode dominates. There also are other regions where both modes coexist, giving the impression of a rectangular pattern (see the discussion of Fig. 4 in Sec. II). The amplitudes of the individual modes can be obtained by complex demodulation as discussed in Sec. II. As an example, the amplitude of the zig mode of the part of the pattern outlined by the square in the top is given in the bottom of Fig. 9 with white representing a

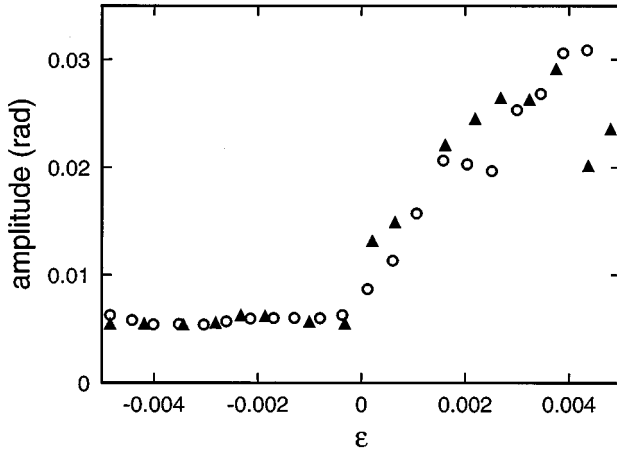


FIG. 8. A typical result of an onset measurement for the EC1 state with  $d=28 \mu\text{m}$ . Here  $\sigma_{\perp}=0.93 \times 10^{-8} \Omega^{-1} \text{m}^{-1}$  and  $T=25 \text{ }^{\circ}\text{C}$ . The circles are the rms deviation of the director from its mean direction while increasing the applied voltage. The triangles are this deviation while decreasing the applied voltage.

large amplitude. It is clear from these images that the correlation lengths of the amplitude parallel and perpendicular to the director are much larger than a roll wavelength. For the example of Fig. 9, this length was determined to be about  $25\lambda$  parallel and  $20\lambda$  perpendicular to the director ( $\lambda=2\pi/|\mathbf{k}|$  is the wavelength of the pattern). To study the temporal correlation, time series of local regions of the pattern were obtained. The four modes are anticorrelated in time, and the correlation time of a given mode [17] was roughly  $1000\tau_d$ . A systematic study of the statistical properties of the EC1 state as a function of  $\epsilon$  and  $\sigma_{\perp}$  has yet to be carried out.

As the conductivity is increased, the primary bifurcation again changes character. Unlike the crossover from worms to EC1, this change appears to occur at a well defined value of  $\sigma_{\perp}$ . As  $\sigma_{\perp}$  is increased, the secondary bifurcation from the EC1 to the SO1 state (see below) is replaced by a transition from the EC1 state to the oblique-roll state. It appears that there must exist a value of  $\sigma_{\perp}$  for which the EC1 to oblique-roll bifurcation line intersects  $\epsilon=0$  (see Fig. 5). Above this value of  $\sigma_{\perp}$ , the primary bifurcation should be to the oblique-roll state. Currently, we have only studied this transition for  $\sigma_{\perp}=2.2 \times 10^{-8} \Omega^{-1} \text{m}^{-1}$  in cell 28-1 (see Fig. 6), and the primary bifurcation was to the SO1 state. A resolution of  $\delta\epsilon=0.01$  was used, and within this resolution, the transition occurs from the conduction state via a large jump in the amplitude of the pattern. Estimates from the power spectra give a change in the rms director amplitude of roughly  $200 \text{ mrad}$  (compare this to Fig. 8), indicating a subcritical bifurcation. Note, the results for this transition are not shown in Fig. 5, which was for cell 28-2, because, as discussed previously, results from two different cells for the  $\epsilon$  values of the secondary bifurcations are not quantitatively comparable.

#### D. EC1 to SO1 to EC2 transition

The transitions between the EC1 and SO1 state and the SO1 state and EC2 states were studied in the most detail. Figure 10 shows single snapshots of the EC1, SO1, and EC2

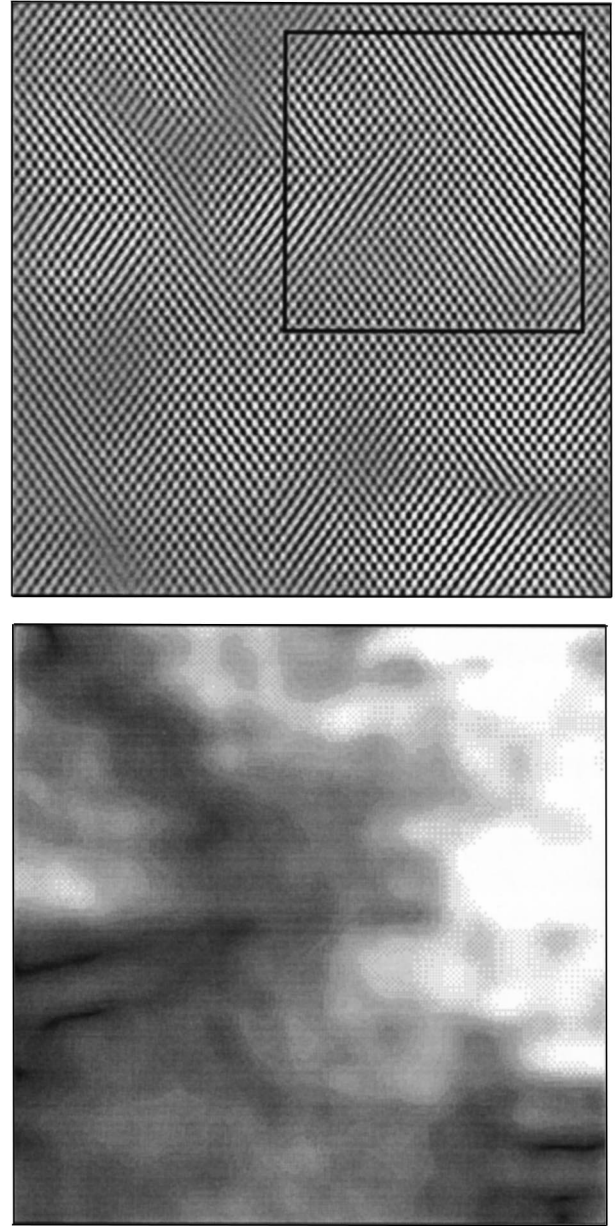


FIG. 9. An example of the EC1 state. The top portion is a real-space image for  $\sigma_{\perp}=1.5 \times 10^{-8} \Omega^{-1} \text{m}^{-1}$ ,  $\epsilon=0.01$ , and  $T=49 \text{ }^{\circ}\text{C}$  covering an area of  $0.35 \text{ cm} \times 0.35 \text{ cm}$  of cell 28-2. The bottom half was obtained by demodulation of the top, and gives the amplitude of the ‘zig’ mode in the  $0.18 \text{ cm} \times 0.18 \text{ cm}$  area shown by the square in the top (dark regions correspond to small and light regions to large amplitudes).

states. Also shown are gray-scale renderings of the corresponding  $S(\mathbf{k}, t)$ . All three states are superpositions of zig and zag rolls with equal  $|\Theta|$ . The differences between the states are the traveling frequencies  $\omega$  of the modes. The EC1 state (a) consists of four modes: right- and left-traveling zig and zag rolls with equal  $|\omega|$ . The SO1 (b) state is the superposition of only two modes: stationary zig and zag rolls ( $\omega=0$ ). The EC2 (c) state consists of six modes: right- and left-traveling zig and zag rolls with equal  $|\omega|$  and stationary zig and zag rolls. Both the EC1 and EC2 states are examples of spatiotemporal chaos. The nonperiodic spatial behavior of these states is evident in Figs. 10(a) and 10(c) as variations

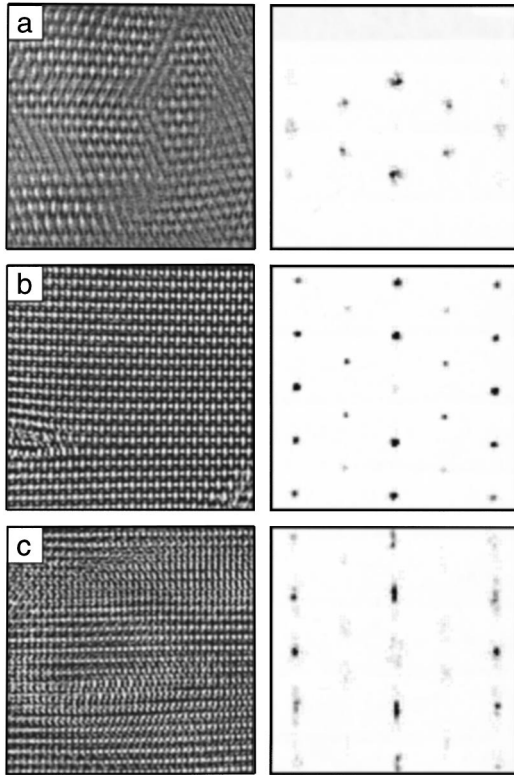


FIG. 10. The left-hand column shows three images from cell 28-2 taken along the dashed arrow of Fig. 5. The images are  $1\text{ mm}\times 1\text{ mm}$ . Image (a) is an example of an EC1 state at  $\epsilon = 0.016$ . (b) is an example of a SO1 state at  $\epsilon = 0.066$ , and (c) is an example of an EC2 state at  $\epsilon = 0.10$ . The right-hand column gives the spatial power spectra  $S(k,t)$  for the corresponding left-hand images. The origins of the spectra are at the image centers, and the spectra cover the range  $-0.3\ \mu\text{m}^{-1} \leq k_x, k_y \leq 0.3\ \mu\text{m}^{-1}$ .

in the amplitudes of the patterns. In contrast, the SO1 state is uniform in space and time except for a few isolated defects, as seen in Fig. 10(b), that travel slowly.

The locations of the transitions were determined by measuring  $\omega$  as a function of  $\epsilon$ . At each step in  $\epsilon$ , a time series of images was taken and  $S(\mathbf{k}, \omega)$  was computed. From  $S(\mathbf{k}, \omega)$ , the traveling-wave frequency was determined. The top part of Fig. 11 is a plot of this frequency as a function of  $\epsilon$  for  $\sigma_{\perp} = 1.0 \times 10^{-8}\ \Omega^{-1}\ \text{m}^{-1}$ . Both the transition from EC1 to SO1 at  $\epsilon = 0.055$  and the transition from SO1 to EC2 at  $\epsilon = 0.080$  occur with a finite jump in frequency. The traveling frequency for the rolls in the EC1 state and EC2 state are of about the same size. For the EC2 state,  $S(\mathbf{k}, \omega)$  has contributions corresponding to  $\omega = 0$  and to  $\omega \approx 0.4\ \text{s}^{-1}$ , showing the presence of traveling *and* stationary rolls.

The behavior of the power in fundamental modes ( $P_{\text{zig}} + P_{\text{zag}}$ , circles) and that in second harmonic modes ( $P_{2\text{zig}} + P_{2\text{zag}} + P_{\text{zig} + \text{zag}} + P_{\text{zig} - \text{zag}}$ , triangles) is shown in the bottom part of Fig. 11. Here  $P_{\text{mode name}}$  refers to the power under the peak in  $S(\mathbf{k})$  that corresponds to the wave vector identified by the mode name, as discussed in Sec. II. As also discussed in Sec. II, the presence of the second harmonics is due primarily to nonlinear optical effects [28]. However, the fundamentals and second harmonics do not exhibit simple behavior. The amplitudes of both the fundamentals and the second harmonics decrease as a function of  $\epsilon$  for the SO1

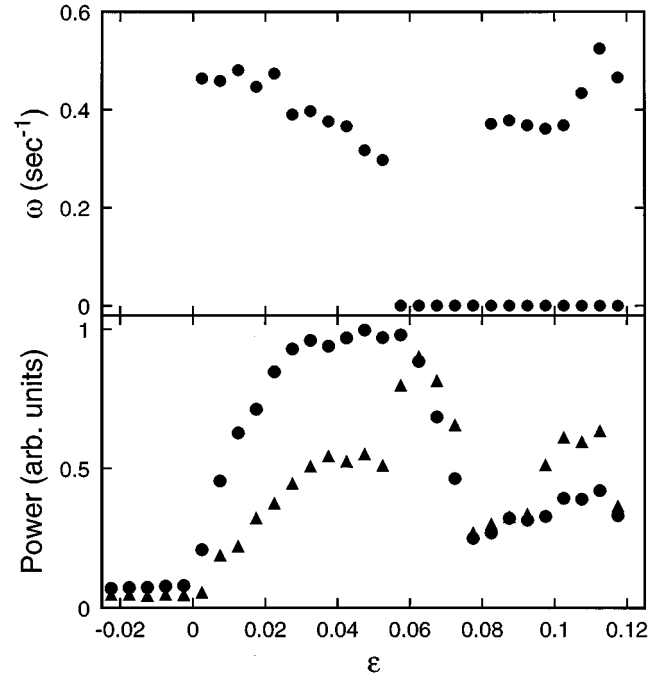


FIG. 11. Top: The traveling-wave frequencies  $\omega$ , measured in cell 28-2, are plotted as a function of  $\epsilon$  for  $\sigma_{\perp} = 1.0 \times 10^{-8}\ \Omega^{-1}\ \text{m}^{-1}$  and  $\Omega\tau_q = 1.34$  (along the dashed arrow in Fig. 5). For  $\epsilon > 0.08$ , both the peak at  $\omega = 0\ \text{s}^{-1}$  and  $\omega \approx 0.4\ \text{s}^{-1}$  have roughly equal amplitudes. Bottom: the corresponding power in fundamental modes (circles) and that in second harmonic modes (triangles) (see text).

state ( $0.055 < \epsilon < 0.08$ ). However, at  $\epsilon = 0.055$ , the second harmonics have a large jump in amplitude, while the fundamentals vary smoothly. This difference of behavior is not understood, and a detailed calculation of the shadowgraph image is necessary to fully elucidate it.

The EC2 state is a highly complicated pattern, and in order to fully characterize its dynamics, one needs to study time series of images covering many spatial correlation lengths. However, limitations of our current apparatus place an upper limit of roughly  $8\lambda$  on the spatial extent of images in a long time series. Qualitative observations of the patterns in real time reveal regions of superimposed stationary zig and zag rolls similar in appearance to the SO1 state. The overall impression is that a nearly uniform SO1 state exists throughout the cell and localized regions of the EC1 state move across this background. One can get a feel for this from Fig. 10(c). In this image, the ‘‘fuzzier’’ regions correspond to places where traveling rolls exist. Regions like the lower left-hand corner [which look like Fig. 10(b)] correspond to places for which the pattern is stationary. Although demodulation of larger images is necessary to show conclusively that the traveling rolls are superimposed over a background pattern which is stationary, demodulations of small images suggest that this is indeed the case.

### E. Additional results

We have not yet quantitatively studied the secondary bifurcations from the worm state as  $\epsilon$  is increased; however, the qualitative features are known. As  $\epsilon$  increases, the num-

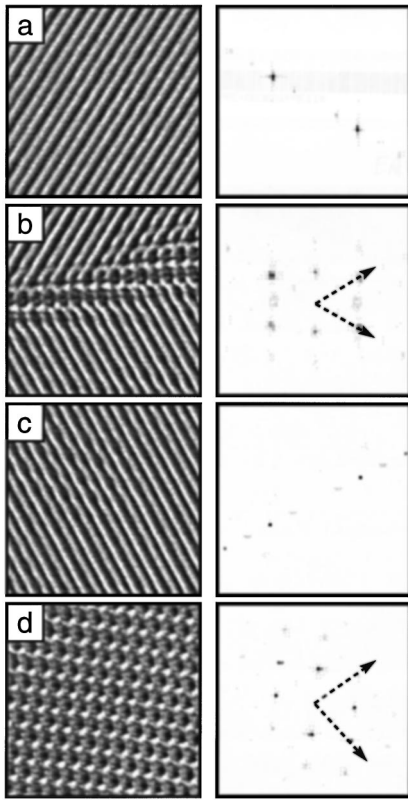


FIG. 12. Four images for cell 28-1 and  $\Omega\tau_q=1.34$  taken from the data corresponding to  $\sigma_{\perp}=2.2\times 10^{-8}\ \Omega^{-1}\ \text{m}^{-1}$  and  $T=44\ ^{\circ}\text{C}$ . The images are (a) an example of the oblique-roll state at  $\epsilon=0.014$ , (b) an example of the oblique-roll state at  $\epsilon=0.067$  showing a grain boundary between zig and zag rolls, (c) an example of the oblique-roll state at  $\epsilon=0.082$ , and (d) an example of the SO2 state at  $\epsilon=0.114$ . Each image covers an area  $0.35\ \text{mm}\times 0.35\ \text{mm}$ . The corresponding gray-scaled images of the spatial power spectra  $S(k,t)$  are shown on the right. For the power spectra, the origins are at the image centers and the spectra cover the range  $-0.6\ \mu\text{m}^{-1}\leq k_x, k_y\leq 0.6\ \mu\text{m}^{-1}$ . The arrows in the spectra are drawn through fundamental peaks. In (b) the angle between them is  $65^{\circ}$ , corresponding to  $|\Theta|=32.5^{\circ}$ . In (d) the angle between the two arrows is close to  $90^{\circ}$ , but the two angles between them and the director (the horizontal) differ from each other.

ber of worms increases, and there is an  $\epsilon$ -dependent spacing between the worms in the  $y$  direction that decreases. The average length of the worms increases as well until, for  $\epsilon\approx 0.1$ , the cell is filled with highly irregular convection. Quantitative studies of this state have not been carried out to determine how it is related to the EC2 state. Given the location of the boundary of the transition to EC2 (see Fig. 5), it is expected that the EC2 state should be observable at low  $\sigma_{\perp}$ . Furthermore, quantitative studies of the transitions as a function of  $\sigma_{\perp}$  (made by sweeping temperature) at constant  $\epsilon>0$  are needed to fully describe the locations of the boundaries of the worm state. In particular, lowering the conductivity from initial states of either EC2 or SO1 are required to complete the bifurcation diagram given in Fig. 5.

The secondary bifurcation from the oblique-roll to the SO2 state involves only the stationary modes. Figure 12 shows four typical images of a small section of the cell 28-1 and their corresponding spatial power spectra as  $\epsilon$  is increased through the oblique-roll to SO2 transition with  $\sigma_{\perp}$

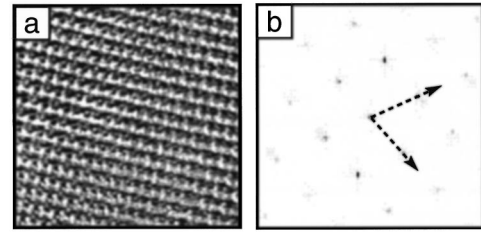


FIG. 13. (a) An image of the SO2 state from cell 28-2 at  $\epsilon=0.17$  with  $\sigma_{\perp}=1.56\times 10^{-8}\ \Omega^{-1}\ \text{m}^{-1}$  and  $T=57\ ^{\circ}\text{C}$ . The image covers a region of  $0.55\ \text{mm}\times 0.55\ \text{mm}$ . (b) The spatial power spectrum of the image. The origin of the spectrum is at the image center, and the spectrum covers the range  $-0.36\ \mu\text{m}^{-1}\leq k_x, k_y\leq 0.36\ \mu\text{m}^{-1}$ . The two arrows in the spectrum are drawn through the fundamental peaks. The angle between them is  $72^{\circ}$ .

$=2.2\times 10^{-8}\ \Omega^{-1}\ \text{m}^{-1}$ . Because of the high values of  $\epsilon$ , the images were dominated by the second harmonics [28]. Therefore, in the spatial power spectra of the images in Fig. 12, the dominant peaks are the result of quadratic effects known to exist for shadowgraph images of EC [28], and the linear peaks are barely visible.

For the case of the oblique-roll state, both the zig and zag rolls often exist in different spatial locations of the cell, separated by grain boundaries. An example of a grain boundary is given in Fig. 12(b), and the corresponding spatial power spectrum shows the degenerate nature of the zig and zag rolls ( $|\Theta_{\text{zig}}|=|\Theta_{\text{zag}}|$ ). In contrast, the spatial power spectrum of the SO2 state [Fig. 12(d)] shows that the two modes are not degenerate. This state nucleates within homogeneous regions of either zig or zag rolls, and not from the grain boundaries between the zig and zag rolls. The angle between the original set of rolls and the rolls which grow as a result of the instability are close to  $90^{\circ}$  in this example [see Fig. 12(d)], but angles as small as  $72^{\circ}$  have been observed. An example showing the smaller angle is illustrated in Fig. 13. Further work is needed to determine the allowable range of angles and the nature of the instability that leads to the superposition of nondegenerate oblique rolls.

#### IV. CONCLUSIONS

We have reported on a survey of patterns which occur in electroconvection in the nematic liquid crystal I52 as a function of three control parameters: applied voltage  $V$ , applied frequency  $\Omega$ , and electrical conductivity  $\sigma_{\perp}$  of the sample. Over the range  $0.8\times 10^{-8}\leq\sigma_{\perp}\leq 1.8\times 10^{-8}\ \Omega^{-1}\ \text{m}^{-1}$ , the initial transition is a supercritical Hopf bifurcation directly to a superposition of degenerate modes which results in a state of spatiotemporal chaos which is extended in space (EC1). For lower values of  $\sigma_{\perp}$ , localized structures known as worms occur above threshold and coexist with the conduction state. For a given set of external parameters, the worms have a unique small width, but a varying and much greater length. The nature of the bifurcation to the worm state needs further elucidation. Immediately above onset, the worms are very rare, but when they do occur they seem to have a finite amplitude. As the conductivity is increased, a codimension-two point is reached beyond which the transition is a subcritical, stationary bifurcation to a single set of stationary oblique rolls.

It is interesting to note that a localized state seemingly similar to our worms was observed by Brand *et al.* [19] for electroconvection in a nematic liquid crystal known as 10E6. Those authors attributed the existence of their state to the fact that their nematic liquid crystal had  $\sigma_{\parallel}/\sigma_{\perp} < 1$ , a condition under which the usual mechanism for electroconvection would be expected to break down. Our samples had  $\sigma_{\parallel}/\sigma_{\perp} > 1$ , and thus we expect that the mechanism for localization would be different in our case.

We also find it interesting that the extended chaos near onset (EC1) observed by us may have been encountered before in experiments by de la Torre and Rehberg [13]. Those authors studied electroconvection in a nematic liquid crystal known as ‘‘Merck Phase V.’’ They observed a supercritical bifurcation from conduction to a small-amplitude traveling oblique-roll state with an ‘‘irregular dynamic cellular structure’’ for a cell of 13- $\mu\text{m}$  spacing. At small driving frequency that state persisted only up to  $\epsilon \approx 0.01$ . With further increase in  $\epsilon$  a hysteretic transition to an oblique-roll state occurred. This sequence is very similar to our observations for  $\sigma_{\perp} \approx 2 \times 10^{-8} \Omega^{-1} \text{ m}^{-1}$ . At larger driving frequency the existence range of the small-amplitude state increased.

Another interesting feature of the EC1 state is the existence of local regions (on the order of a spatial correlation length) for which the four modes had roughly equal amplitudes and the pattern was a superposition of zig and zag *standing* waves. Because of the rather long correlation times, these regions tend to be relatively robust. In general, the two standing waves were one-quarter of a cycle out of phase with each other, resulting in a state that alternates between zig and zag rolls. A short time series of images of the resulting pattern is shown in Fig. 14. This *locally* occurring feature of the pattern is interesting because of the strong similarity to a solution of coupled amplitude equations appropriate to a system of superimposed, traveling oblique rolls with *no spatial variation of the amplitude* studied by Silber *et al.* (see Fig. 2 of Ref. [31]; there the solution is referred to as alternating rolls). To describe the full spatial behavior of the EC1 state, the equations used in Ref. [31] need to be modified to include the spatial variation of the pattern. In principle, such equations can be derived from the weak-electrolyte model which has already successfully explained the linear properties of the system [20].

A number of interesting secondary bifurcations involving the interaction of traveling and stationary oblique rolls were observed. We discussed in some detail the transition from the EC1 to the SO1 to the EC2 state and the transition from the oblique-roll to the SO2 state. The EC1-SO1-EC2 transitions consist of a secondary bifurcation from a state of spatiotemporal chaos to a time-independent spatially uniform state which is followed by a transition back to a state of spatiotemporal chaos. The EC2 state appears to be the superposition of a uniform stationary state with patches of a state of spatio-temporal chaos consisting of traveling rolls. The transition from the oblique-roll state to the SO2 state represents an instability involving the superposition of nondegenerate oblique rolls.

The equations of motion of electroconvection, the weak-electrolyte model [21], have been well established and potentially allow for close contact between theory and experiment. The linear parameters associated with the Hopf

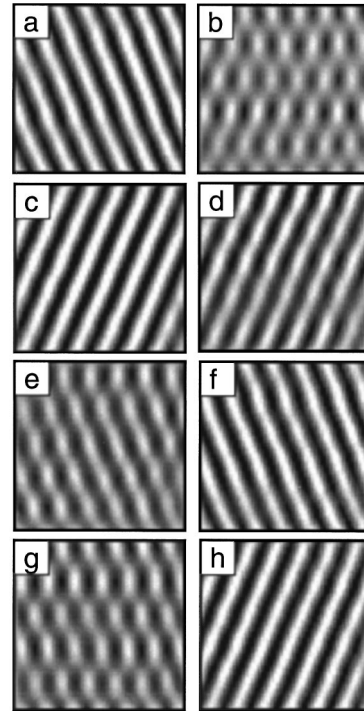


FIG. 14. A time series of images of a local region of the EC1 state covering an area of  $0.3 \text{ mm} \times 0.3 \text{ mm}$  for cell 28-1. These results are for  $\Omega \tau_q = 1.37$ ,  $\sigma_{\perp} = 1 \times 10^{-8} \Omega^{-1} \text{ m}^{-1}$ ,  $T = 25 \text{ }^{\circ}\text{C}$ , and  $\epsilon = 0.005$ . The images (a)–(h) were taken roughly 1 s apart, respectively, and demonstrate that the state alternates between zig and zag rolls.

bifurcation  $(\omega_c, \mathbf{k}_c, V_c)$  already have been explained quantitatively by the weak-electrolyte model [20]. In principle, it is possible to derive coupled complex Ginzburg-Landau equations, one for each mode, from the weak-electrolyte model. These equations should describe the nonlinear aspects of the system quantitatively for small values of  $\epsilon$  and over the parameter range where the primary bifurcation is supercritical. This theoretical approach should be applicable particularly to the EC1 state, and possibly may also lead to an elucidation of the localized worm state. Some theoretical progress in this direction has already been made [32]. Solutions to the complex Ginzburg-Landau equations would be useful both when trying to select interesting values of the parameters and for deepening our understanding of the spatiotemporal chaos reported here.

In the large parameter space that is involved, a wide range of phenomena occur. The existence of the firm theoretical foundation provided by the weak-electrolyte model makes the further pursuit of many of them particularly interesting. Here we mention a few. The various bifurcation lines need to be studied in more detail as a function of  $\Omega \tau_q$ ,  $\sigma_{\perp}$ , and cell spacing  $d$ . Particularly important seems to be an elucidation of the nature of the primary bifurcation to the worm state. The mechanism responsible for the oblique roll to SO2 transition also is not understood, and this unusual transition deserves further quantitative examination. There is a point in parameter space where the states SO2, oblique roll, SO1, and EC2 appear to meet or come very close to each other. The interactions of these four patterns may result in interesting behavior in the neighborhood of this point. The behavior of

the system near the codimension-two point where the EC1 to oblique-roll transition intersects the initial bifurcation is also of interest. At this point, the initial bifurcation changes from a supercritical Hopf to a subcritical stationary bifurcation.

Perhaps of greatest interest is the nature of the two states of spatiotemporal chaos that occur immediately above onset, namely, the worm state and the EC1 state. Their statistical properties should be studied quantitatively, so that a comparison with quantitative theoretical calculations can be made. Further, there is the issue of the nature of the third state of spatiotemporal chaos, EC2. Is it simply the superposition of EC1 and SO1, or is it an example of spatiotemporal chaos that is distinct from the EC1 state?

The new patterns reported here involved the interactions between oblique rolls possessing relatively large values of  $\Theta$ . A deeper understanding of pattern formation in aniso-

tropic systems requires a more comprehensive study of the connection between the value of  $\Theta$ , the nature of the interactions between oblique rolls, and the resulting nonlinear patterns. Electroconvection is an ideal system for such a study because there is a large number of external parameters which affect the interactions between the degenerate oblique rolls. For example, grid patterns similar in appearance to the SO1 state have been observed previously under the application of combined ac and dc electric fields [33]. Also,  $\Theta$  can easily be varied by changing  $\epsilon_a$ ,  $\Omega$ , and by applying external magnetic fields.

#### ACKNOWLEDGMENT

This work was supported by the National Science Foundation through Grant No. DMR94-19168.

- 
- [1] A large literature pertaining to this field has evolved. Useful reviews are given by F. Busse, in *Hydrodynamic Instabilities and the Transition to Turbulence*, edited by H. L. Swinney and J. P. Gollub (Springer, Berlin, 1981), p. 97; Rep. Prog. Phys. **41**, 1929 (1978).
- [2] For a recent review, see M. C. Cross and P.C. Hohenberg, Rev. Mod. Phys. **65**, 851 (1993).
- [3] For a recent review of pattern formation in liquid crystals, see L. Kramer and W. Pesch, Annu. Rev. Fluid Mech. **27**, 515 (1995).
- [4] E. Bodenschatz, W. Zimmermann, and L. Kramer, J. Phys. (France) **49**, 1875 (1988); L. Kramer, E. Bodenschatz, W. Pesch, W. Thom, and W. Zimmermann, Liq. Cryst. **5**, 699 (1989).
- [5] W. Zimmermann, in *Nematics: Mathematical and Physical Aspects*, Vol. 332 of *NATO Advanced Study Institute, Series C: Mathematical & Physical Sciences*, edited by J.-M. Coron, J. M. Ghidaglia, and F. Helein (Kluwer Academic Publishers, Dordrecht, 1991), p. 401.
- [6] I. Rehberg, B. L. Winkler, M. de la Torre Juárez, S. Rasenat, and W. Schöpf, Festkörperprobleme **29**, 35 (1989).
- [7] See, for instance, L. M. Blinov, *Electro-Optical and Magneto-Optical Properties of Liquid Crystals* (Wiley, New York, 1983).
- [8] R. Ribotta, A. Joets, and L. Lin, Phys. Rev. Lett. **56**, 1595 (1986).
- [9] S. Kai and K. Hirakawa, Prog. Theor. Phys. Suppl. **64**, 212 (1978).
- [10] A. Joets and R. Ribotta, Phys. Rev. Lett. **60**, 2164 (1988).
- [11] I. Rehberg, S. Rasenat, and V. Steinberg, Phys. Rev. Lett. **62**, 756 (1989).
- [12] I. Rehberg, S. Rasenat, M. de la Torre Juárez, and V. Steinberg, Phys. Rev. Lett. **61**, 2449 (1988).
- [13] M. de la Torre Juárez and I. Rehberg, Phys. Rev. A **42**, 2096 (1990).
- [14] M. Dennin, D.S. Cannell, and G. Ahlers, Mol. Cryst. Liq. Cryst. **261**, 377 (1995).
- [15] M. Dennin, G. Ahlers, and D. S. Cannell, in *Spatio-Temporal Patterns*, edited by P. E. Cladis and P. Muhoray (Addison-Wesley, Reading, MA, 1994), p. 353.
- [16] A. Joets, X. D. Yang, and R. Ribotta, Physica D **23**, 235 (1986).
- [17] M. Dennin, G. Ahlers, and D. S. Cannell, Science **272**, 388 (1996).
- [18] M. Dennin, G. Ahlers, and D. S. Cannell, Phys. Rev. Lett. **77**, 2475 (1996).
- [19] H.R. Brand, C. Fradin, P.L. Finn, W. Pesch, and P.E. Cladis, Phys. Lett. A **235**, 508 (1997).
- [20] M. Dennin, M. Treiber, L. Kramer, G. Ahlers, and D. S. Cannell, Phys. Rev. Lett. **76**, 319 (1996).
- [21] M. Treiber and L. Kramer, Mol. Cryst. Liq. Cryst. **261**, 311 (1995).
- [22] J. R. deBruyn, E. Bodenschatz, S. Morris, S. Trainoff, Y.-C. Hu, D.S. Cannell, and G. Ahlers, Rev. Sci. Instrum. **67**, 2043 (1996).
- [23] M. Dennin, Ph.D. thesis, University of California at Santa Barbara, 1995.
- [24] Many other dopants were tried (see Ref. [23]), but only  $I_2$  yielded a sufficiently high conductivity to permit convection.
- [25] U. Finkenzeller, T. Geelhaar, G. Weber, and L. Pohl, Liq. Cryst. **5**, 313 (1989).
- [26] S. W. Morris, E. Bodenschatz, D. S. Cannell, and G. Ahlers, Phys. Rev. Lett. **71**, 2026 (1993).
- [27] M. A. Dominguez-Lerma, G. Ahlers, and D. S. Cannell, Phys. Rev. E **52**, 6159 (1995).
- [28] S. Rasenat, G. Hartung, B. L. Winkler, and I. Rehberg, Exp. Fluids **7**, 412 (1989).
- [29] For  $I_2$  over the range of temperatures used here,  $\epsilon_0 \epsilon_{\perp} \approx 2.6 \times 10^{-11} \Omega^{-1} \text{ m}^{-1} \text{ s}$ , where  $\epsilon_0$  is the permittivity of free space and  $\epsilon_{\perp}$  is taken from Ref. [25].
- [30] I. Rehberg, S. Rasenat, M. de la Torre-Juarez, W. Schöpf, F. Hörner, G. Ahlers, and H. R. Brand, Phys. Rev. Lett. **67**, 596 (1991).
- [31] M. Silber, H. Riecke, and L. Kramer, Physica D **61**, 260 (1992).
- [32] M. Treiber, Ph.D. thesis, Universität Bayreuth, Bayreuth, Germany, 1996 (unpublished); and private communication.
- [33] S. Kai, Y. Adachi, and S. Nasuno, in *Spatio-Temporal Patterns*, edited by P. E. Cladis and P. Muhoray (Addison-Wesley, Reading, MA, 1994), p. 313.